Argon metastable densities in radio frequency Ar, Ar/O_2 and Ar/CF_4 electrical discharges

Shahid Rauf[a] and Mark J. Kushner[b]
Department of Electrical and Computer Engineering, University of Illinois, 1406 West Green Street, Urbana, Illinois 61801

(Received 19 March 1997; accepted for publication 11 June 1997)

The spatial distributions of excited states in radio frequency electrical gas discharges have been observed to be dynamic functions of gas mixture, pressure, and applied voltage. Recent measurements of two-dimensional profiles of excited states in the Gaseous Electronics Conference reference cell (GECRC) [McMillin and Zachariah, J. Appl. Phys. **77**, 5538 (1995); **79**, 77 (1996)] have shown that the spatial distribution of the Ar($4s$) density varies considerably with operating conditions. The peak density of Ar($4s$) systematically shifted in position, as well as changed in magnitude, with variations in pressure, applied voltage, and gas mixture. In this article, we present results from a two-dimensional computer simulation of Ar, Ar/O_2, and Ar/CF_4 discharges sustained in the GECRC with the intent of investigating the experimental trends. The simulations, performed with the Hybrid Plasma Equipment Model, agree well with experiments. They show that the shift in Ar($4s$) densities is largely explained by the reduction in the electron mean free path, and local perturbations in the ambipolar electric field resulting from electrode structures. Additions of small amounts of O_2 and CF_4 decrease the Ar($4s$) density due to quenching, and change its profile due to a transition to an electronegative plasma. © *1997 American Institute of Physics.* [S0021-8979(97)02518-8]

I. INTRODUCTION

Capacitively coupled gas discharges are common plasma tools in the microelectronics fabrication industry for depositing thin films, and etching metals and semiconductors. Experimental observations of excited atomic and molecular states in these devices have shown highly nonuniform distributions in spite of the geometry, a parallel plate discharge, being fairly simple. For example, recent experiments in the Gaseous Electronics Conference reference cell (GECRC)[1] by McMillin and Zachariah[2–4] have shown that excited state species are a dynamic function of gas mixture, gas pressure, applied voltage, and other operating conditions. In these experiments, laser induced florescence (LIF) was used to map two-dimensional (2D) profiles of excited state argon [Ar($4s$)] densities in Ar, Ar/O_2, Ar/CF_4, and Ar/Cl_2 plasmas. It was found that in pure Ar the axial Ar($4s$) density distribution is almost symmetric between the electrodes at low pressure (100 mTorr). The magnitude of the Ar($4s$) density varied as a function of radius with the peak density occurring close to the edge of the electrodes. As the pressure was increased to 1 Torr, the Ar($4s$) density increased, the peak in density shifted towards the powered electrode, and a visible skew appeared in the profile. At low pressure (100 mTorr), varying voltage did not significantly affect the shape of the profile, whereas at 1 Torr, an increase in voltage led to a tighter collapse of the peak of the Ar($4s$) density to near the powered electrode. Addition of up to 2% O_2 to Ar led to a monotonic decrease in the Ar($4s$) density while there was otherwise no significant change in the shape of the profile. When CF_4 was added to Ar, the decrease in the Ar($4s$) density was significantly less than it was with comparable additions of O_2. However, at high concentrations of CF_4 (3.6%), the peak in Ar($4s$) density shifted towards the powered electrode. Off axis peaks in both electron density and excited state densities have also been observed by electric probe measurements and in simulations.[5,6] The observations have been largely attributed to electric field enhancement at the edges of the electrodes.

To investigate the physical processes responsible for these observations, and comment more generally on the disposition of excited states in rf discharges, we have simulated the experiments of McMillin and Zachariah[2–4] using the hybrid plasma equipment model (HPEM).[7–9] The HPEM is a 2D simulation of capacitively coupled discharges, which employs a hybrid approach in which electron transport is addressed either hydrodynamically or kinetically, and a fluid simulation containing various levels of detail is used for the heavy particles. By utilizing these options for electron and heavy particle transport, we have also gained some insight into the level of modeling complexity required to address the observed physical phenomena.

We found that the 2D profiles of the Ar($4s$) density produced while varying voltage and pressure in argon discharges can all be explained in terms of a combination of electric field enhancement and the electron mean free path. Ar($4s$) is generated primarily through electron impact excitation by sheath heated electrons. At low pressure, the electron mean free path is comparable to the electrode separation and so excitation of Ar($4s$) occurs throughout the gap. With the mean free path for quenching also being larger than the gap, the Ar($4s$) is consequently symmetrically distributed between the electrodes. At higher pressure, the mean free path of sheath heated electrons decreases, localizing excitation near the powered electrode. The rate of quenching of

[a]Electronic mail: rauf@uigela.ece.uiuc.edu
[b]Electronic mail: mjk@uiuc.edu

Ar($4s$) by heavy particle and electron collisions also increases, thereby further restricting its density to being adjacent to the powered electrode where it is being generated. Electric field enhancement at the edge of the electrodes contributes to this shift. The decrease in Ar($4s$) density when O_2 is added is mainly due to the quenching of Ar($4s$) by O_2 and O while the spatial distribution of its density is not strongly affected. In a similar manner, CF_4 and C_2F_6 quench Ar($4s$) in Ar/CF_4, leading to a decrease in its density. The change in Ar($4s$) profile due to the addition of CF_4 is further linked to a spatially inhomogeneous loss of electrons through attachment.

The HPEM as used in this study is described in Sec. II. The effects of pressure, applied voltage, and addition of trace amounts of O_2 and CF_4 on Ar($4s$) density profiles are examined in Sec. III. Remarks on the appropriate modeling technique for simulating these devices are in Sec. IV. Our concluding remarks are in Sec. V.

II. DESCRIPTION OF THE MODEL

The simulations described in this article were performed using the HPEM. The HPEM has been previously described in Refs. 7–10, and so will be only briefly discussed here. It consists of three sets of modules. The first module deals with computing inductively coupled electromagnetic fields in which Maxwell's equations are solved, as are circuit equations for the rf circuitry and antennas. The second is the electron energy transport module (EETM). The options in this module include an electron Monte Carlo simulation (EMCS) and solution of the electron energy equation coupled with a solution of Boltzmann's equation. These modules generate source functions for electron impact reactions and electron transport coefficients. In the third module, the fluid-kinetics module (FKM), densities and fluxes for charged and neutral species are computed, and Poisson's equation is solved for the electric potential. A circuit model is also employed to obtain dc biases on powered substrates. Heavy particle transport is handled by solving either continuity and momentum equations, or only the continuity equation using drift-diffusion approximations. The coupled modules of the HPEM are solved iteratively until quasi-steady state conditions are obtained. Since we are simulating a capacitively coupled plasma reactor, only the EETM and FKM are used here. Gas flow from a showerhead nozzle to the pump ports is included.

In this work, we are addressing rf discharges sustained in Ar, and in Ar/O_2 and Ar/CF_4 mixtures. The species and reactions included in the model are listed in Tables I, II, and III. The Ar/O_2 and Ar/CF_4 reaction sets also contain the basic Ar reactions listed in Table I. We performed simulations over a large range of conditions having a more complex model for Ar which included the Ar($4p$) manifold. We found that there were only nominal differences in all densities and discharge parameters compared to the simpler model containing only Ar($4s$), denoted herein as Ar*.

In defining Ar*, we lumped together the four sublevels of Ar($4s$). In reality, two of these sublevels are radiatively coupled to the ground state, whereas the other two are metastable. We compensate for the decay of the radiative states with a radiation trapping model. Using the Holstein formulation,[11] we account for trapping by multiplying the spontaneous emission coefficient of the radiative states by the escape factor

$$g = 1.875[k_0 L(\pi \log \tfrac{1}{2} k_0 L)^{1/2}]^{-1}, \tag{1}$$

where L is the scale length of the plasma and k_0 is defined for Doppler broadening as

TABLE I. Ar reaction set.[a]

Species Ar, Ar*, Ar^+, e Reaction	Rate Coefficient[b]	Reference
$e+Ar \leftrightarrow Ar^*+e$	c	13
$e+Ar \rightarrow Ar^+ + e + e$	c	14
$e+Ar^* \rightarrow Ar^+ + e + e$	c	15
$Ar^*+Ar^* \rightarrow Ar^+ + Ar + e$	5×10^{-10}	16
$Ar^* \rightarrow Ar$	d	

[a]Only reactions directly affecting species densities are shown here. Additional electron impact collisions (e.g., momentum transfer) are included in the EETM.
[b]Rate coefficients have units of $cm^3\,s^{-1}$ unless noted otherwise.
[c]Computed using the electron energy distribution and electron impact cross section from cited reference.
[d]This reaction takes into account the decay of the radiative Ar($4s$) sublevels. See text.

TABLE II. Additional reactions and species for Ar/O_2 plasmas.[a]

Species O_2, O_2^+, $O_2^*[O_2(^1\Delta)]$, O, O*[O(^{1}D)], O^+, O^- Reaction	Rate coefficient[b]	Reference
$e+O_2 \rightarrow O^- + O$	c	17
$e+O_2 \rightarrow O_2^* + e$	c	17
$e+O_2 \rightarrow O^* + O + e$	c	17
$e+O_2 \rightarrow O + O + e$	c	17
$e+O_2 \rightarrow O_2^* + e + e$	c	17
$e+O_2^+ \rightarrow O^* + O$	1.0×10^{-8}	18[d]
$e+O \rightarrow O^* + e$	c	19
$e+O \rightarrow O^+ + e + e$	c	19
$e+O^* \rightarrow O + e$	c	19
$e+O^* \rightarrow O^+ + e + e$	c	19
$O^-+O_2^+ \rightarrow O + O_2$	1.0×10^{-7}	20[d]
$O^-+O^+ \rightarrow O + O$	1.0×10^{-7}	20[d]
$O^-+O \rightarrow O_2 + e$	3.0×10^{-10}	21
$O^-+O_2^+ \rightarrow O + O + O$	1.0×10^{-7}	20[d]
$O^+ + O_2 \rightarrow O + O_2^+$	1.0×10^{-11}	22
$O^* + O \rightarrow O + O$	8.0×10^{-12}	23[d]
$O^* + O_2 \rightarrow O + O_2^*$	1.0×10^{-12}	23
$O^* + O_2 \rightarrow O + O_2$	3.8×10^{-11}	24
$Ar^+ + O_2 \rightarrow O_2^+ + Ar$	5.1×10^{-11}	25
$Ar^+ + O \rightarrow O^+ + Ar$	6.4×10^{-12}	26
$Ar^* + O_2 \rightarrow O + O^* + Ar$	2.1×10^{-10}	27
$Ar^* + O \rightarrow O^* + Ar$	4.1×10^{-11}	28

[a]Only reactions directly affecting species densities are shown here. Additional electron impact collisions (e.g., momentum transfer, vibrational excitation) are included in the EETM.
[b]Rate coefficients have units $cm^3\,s^{-1}$.
[c]Computed using the electron energy distribution and electron impact cross sections from cited reference.
[d]Estimated. See cited reference for similar reaction.

TABLE III. Additional reactions and species for Ar/CF_4 plasmas.[a]

Species		
CF_4, CF_3, CF_3^+, CF_3^-, CF_2, CF, F, F^-, F_2, C_2F_3, C_2F_4, C_2F_6		
$e+CF_4 \rightarrow CF_3+F+e$	c	29
$e+CF_4 \rightarrow CF_2+F+F+e$	c	29
$e+CF_4 \rightarrow CF+F+F_2+e$	c	29
$e+CF_4 \rightarrow CF_3^++F+e+e$	c	29
$e+CF_4 \rightarrow CF_3+F^-$	c	29
$e+CF_4 \rightarrow CF_3^-+F$	c	29
$e+CF_4 \rightarrow CF_3^++F^-+e$	c	29
$e+CF_3 \rightarrow CF_2+F+e$	c	29[d]
$e+CF_3 \rightarrow CF_2+F^-$	c	29[d]
$e+C_2F_6 \rightarrow CF_3+CF_3+e$	c	30
$e+C_2F_6 \rightarrow CF_3^++CF_3+e+e$	c	30
$e+C_2F_6 \rightarrow CF_3+CF_3^-$	c	30
$e+C_2F_4 \rightarrow CF_2+CF_2+e$	c	30[e]
$e+C_2F_4 \rightarrow F^-+C_2F_3$	c	30[e]
$e+F_2 \rightarrow F^-+F$	c	31
$e+F_2 \rightarrow F+F+e$	c	31
$CF_3^-+F \rightarrow CF_3+F^-$	5.0×10^{-8}	32
$CF_3^-+Ar^+ \rightarrow CF_3+Ar$	1.0×10^{-7}	20
$CF_3^-+CF_3^+ \rightarrow CF_3+CF_3$	1.0×10^{-7}	20
$F^-+Ar^+ \rightarrow F+Ar$	1.0×10^{-7}	20
$F^-+CF_3^+ \rightarrow F+CF_3$	1.0×10^{-7}	20
$Ar^++CF_4 \rightarrow CF_3^++F+Ar$	9.58×10^{-10}	33[f]
$Ar^*+CF_4 \rightarrow CF_2+F_2+Ar$	6.0×10^{-11}	34
$Ar^*+C_2F_6 \rightarrow CF_3+CF_3+Ar$	4.0×10^{-11}	34
$CF+F+M \rightarrow CF_2+M$	6.96×10^{-29} $cm^6\ s^{-1}$	35
$CF_2+F_2 \rightarrow CF_3+F$	4.56×10^{-13}	36
$CF_2+CF \rightarrow C_2F_3$	1.0×10^{-12}	37
$CF_2+CF_2 \rightarrow C_2F_4$	5.0×10^{-14}	37
$CF_3+F_2 \rightarrow CF_4+F$	1.88×10^{-14}	36
$CF_3+CF_3+M \rightarrow C_2F_6+M$	3.94×10^{-29} $cm^6\ s^{-1}$	35
$C_2F_3+F \rightarrow C_2F_4$	1.0×10^{-12}	37
$C_2F_4+F \rightarrow CF_3+CF_2$	4.0×10^{-11}	37
$C_2F_5+F \rightarrow CF_3+CF_3$	1.0×10^{-11}	37
$F+F+M \rightarrow F_2+M$	6.77×10^{-28} $cm^6\ s^{-1}$	35

[a]Only reactions directly affecting species densities are shown here. Additional electron impact collisions (e.g., momentum transfer, vibrational excitation) are included in the EETM.

[b]Rate coefficients have units $cm^3\ s^{-1}$ unless noted otherwise. M is any third body.

[c]Computed using the electron energy distribution and electron impact cross sections from cited reference.

[d]Estimated by analogy to CF_4.

[e]Estimated by analogy to C_2F_6.

[f]Value is the maximum in the range of uncertainty.

$$k_0=\frac{\lambda_0^3 N}{8\pi}\frac{g_1}{g_2}\frac{\gamma}{\pi^{1/2}\nu_0}. \tag{2}$$

The variables λ_0, N, γ, and ν_0 are, respectively, the radiation wavelength, the ground state density of the transition, the spontaneous emission coefficient, and the atom thermal speed. The effective radiative lifetime for Ar* was computed in the following manner. We first computed the effective radiative rate for the individual states. We then constructed a collisional radiative model for the four sublevels of the $Ar(4s)$ manifold and ground state including electron and heavy particle mixing of the multiplex. The effective radiative relaxation rate for Ar* is obtained by multiplying and summing each sublevel's radiative rate by its relative population. It is somewhat debatable whether the escape of radiation excitation is governed by Doppler or collisional broadening in the relevant parameter regime. We therefore also used another Ar model in which collisional broadening was considered while taking account of radiative states. The Ar* densities obtained using this model or the one with Doppler broadening, however, do not differ by more than 3%. The results described in this article are for the Doppler broadening model.

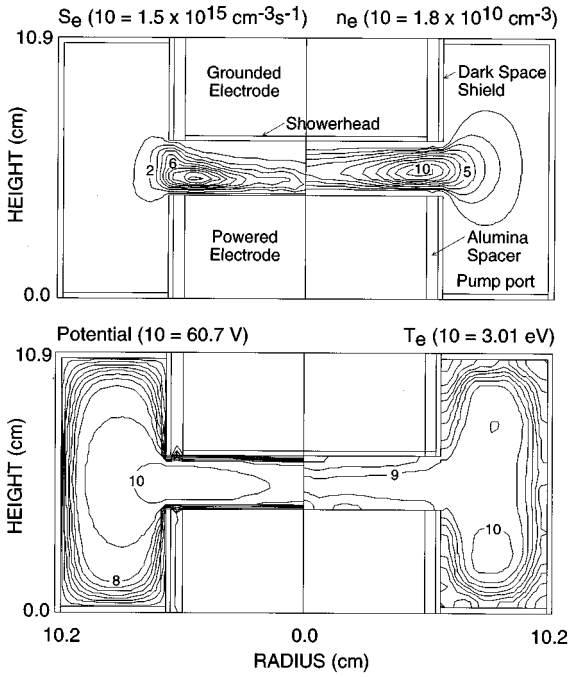

FIG. 1. Electron source function S_e, electron density n_e, plasma potential and electron temperature T_e for an Ar discharge (250 mTorr, 200 V_{p-p}) in the GECRC. The bottom electrode is powered. The top electrode and chamber are grounded.

III. SPATIALLY DEPENDENT EXCITED STATE DENSITIES

The computational geometry used in the study is shown in Fig. 1. The GECRC consists of two parallel electrodes separated by 2.26 cm and which are 5.1 cm in radius. The top electrode is grounded while an rf voltage at 13.56 MHz is applied to the bottom electrode. The electrodes are surrounded by a 0.16-cm-thick alumina spacer and a 0.1-cm-thick metal dark space shield layer. The feedstock gas is flowed into the chamber through a showerhead nozzle in the top electrode. The exhaust gases are pumped out at the bottom of the chamber. The gas flow rates in Ar, Ar/O_2, and Ar/CF_4 are 10, 25, and 25 sccm, respectively. The alumina spacer and dark space shield are slightly smaller in height than the electrode. The mesh we used for Ar and Ar/O_2 simulations does not resolve this difference. It was, however, found necessary to refine the mesh and resolve these steps for simulation of the Ar/CF_4 mixture.

The HPEM has been validated in a variety of reactor configurations. In this study, validation was performed by comparing predicted line integrated average electron densities with experiments.[12] The results are shown in Fig. 2. Electron densities are relatively constant at low pressures

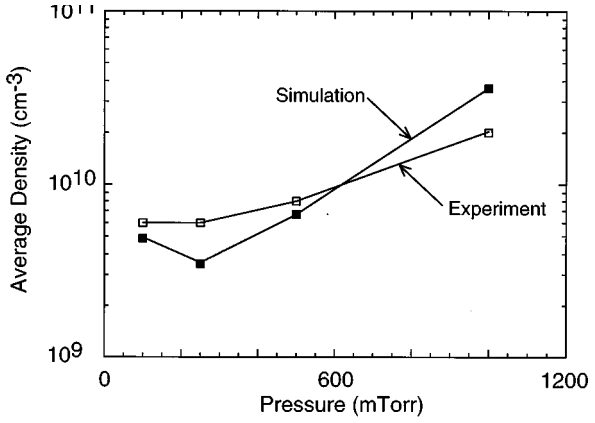

FIG. 2. Comparison of the average electron density obtained from the model and experiments.

(<200 mTorr) and increase at higher pressures. Over the range of 100–1000 mTorr, the model agrees with the experiments within a factor of 2.

The electron density n_e, electron temperature T_e, electron source S_e, and plasma potential are shown in Fig. 1 for Ar at 250 mTorr, applied potential of 200 V_{p-p} and flow rate of 10 sccm. The dc bias is -81 V. The electron source function is maximum near the edges of the electrodes with an axial shift towards the powered electrode due to sheath heated electrons. The source function for Ar* has essentially the same shape as S_e. Electric field enhancement at the edge of the electrodes, which generates additional sheath heating, produces the radial extrema in the electron source function and the shift in the extrema towards the powered electrode. The average electron temperature varies only slightly in the gap. Note that there is a local maximum in electron temperature outside the gap near corners where converging sheaths produce a large heating rate. The variation in source function results dominantly from a time dependent modulation in the tail of the electron distribution function which is not apparent in the average temperature. The large spatial variation in source function while the bulk electron temperature is nearly constant requires a kinetic treatment of electron transport which can resolve modulation in the shape of the electron energy distribution. The electrons diffuse in the axial direction from their site of generation, and the peak in electron density occurs slightly above the maximum in S_e.

The computed Ar* density at Ar pressures of 100, 250, 500, and 1000 mTorr are shown in Fig. 3 for 200 V_{p-p}. For comparison, we have also included the experimental results of McMillin and Zachariah[2] in Fig. 4. The Ar* density as a function of height at the centerline is shown in Fig. 5(a). The simulation and experimental results agree reasonably well throughout the pressure range. At 100 mTorr, Ar* is distributed fairly symmetrically in the axial direction between the electrodes. The Ar* density has a radial peak near the edge of the electrodes, commensurate with the source function. This profile is similar to that for the electron density at 100 mTorr. The similarity in profiles is not surprising since the major source of Ar* is electron impact excitation whose distribution is essentially the same as ionization. As long as transport is diffusion dominated, the two profiles should be similar.

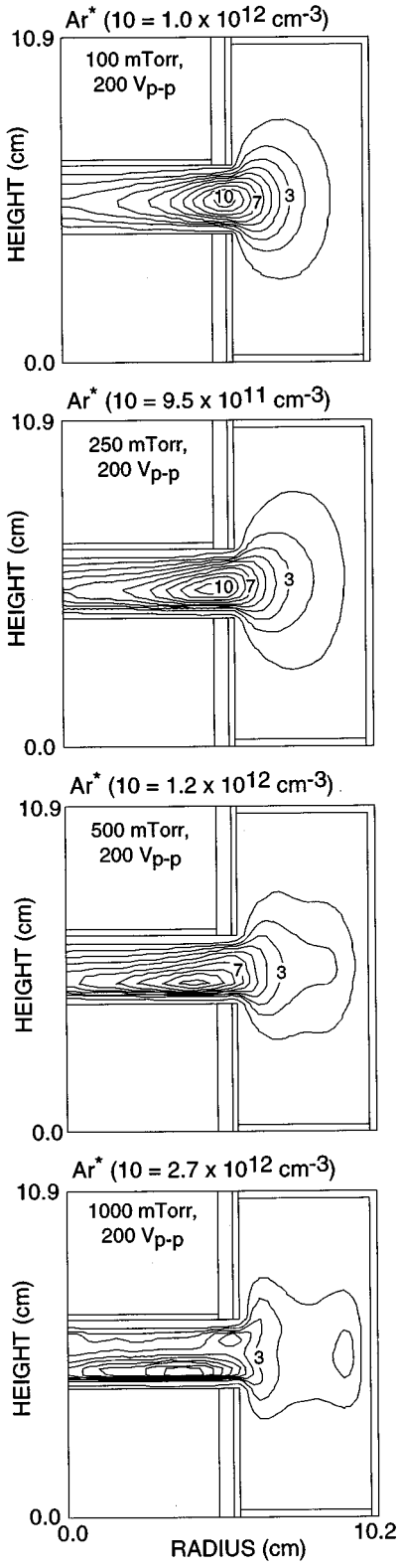

FIG. 3. Computed Ar* density in pure argon plasmas for an applied voltage of 200 V_{p-p}. (a) 100 mTorr, (b) 250 mTorr, (c) 500 mTorr, and (d) 1000 mTorr.

As the pressure is increased to 250 mTorr the peak in Ar* density shifts slightly towards the powered electrode

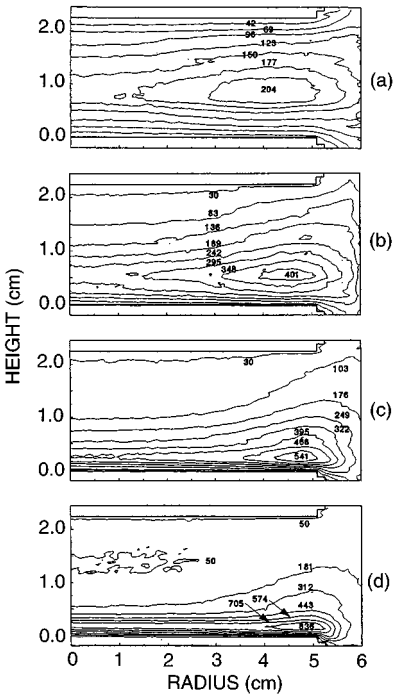

FIG. 4. Experimental Ar* density in pure argon plasmas for an applied voltage of 200 $V_{p\text{-}p}$. (a) 100 mTorr, (b) 250 mTorr, (c) 500 mTorr, and (d) 1000 mTorr. Densities are relative values obtained from Ref. 2.

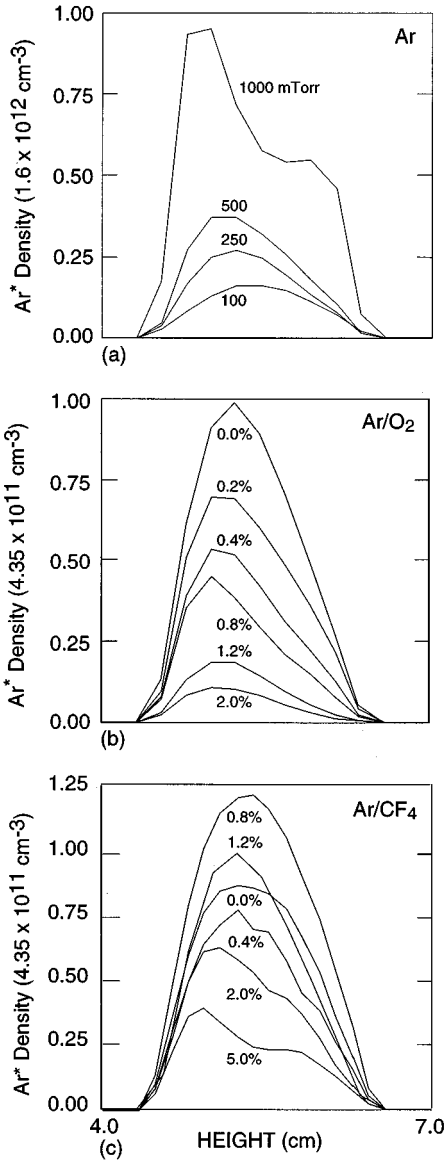

FIG. 5. Axial profile of Ar* density in the center of the reactor as a function of: (a) pressure in Ar, (b) O_2 addition in Ar, and (c) CF_4 addition in Ar. The labels for the Ar/O_2 and Ar/CF_4 are percent of the additive.

and a noticeable skew appears in the profile. When the pressure is increased further to 500 mTorr, the Ar* density peaks more closely to the powered electrode and the skew is more apparent. At 1000 mTorr, the Ar* density peaks at the corner of the powered electrode in the experiment, though less so in the simulation. We, in addition, find a secondary peak in Ar* density at the edge of the top electrode at 1000 mTorr in the simulation. This secondary peak might be a consequence of our finite mesh size which may not resolve the electric field sufficiently. We have, however, not been able to resolve the precise cause for the secondary peak in our simulation yet.

The shift in Ar* towards the powered electrode and its skew towards the corner of the electrode as the pressure increases results primarily from the reduction in electron mean free path and increase in quenching of Ar*. As the gas pressure increases, the electron mean free path decreases while the electron density increases. Sheath heated electrons at the powered electrode therefore dissipate their energy through excitation closer to the electrode. The increase in electron density reduces the sheath thickness and sheath velocity, thereby producing less energetic sheath heated electrons, which in turn have a shorter energy dissipation length. As the sheath (and presheath) collapse, the electric field enhancement at the edge of the electrode becomes more pronounced, leading to the larger skew in the Ar* profile.

Computed Ar* densities for 75 and 300 V_{p-p} applied voltage at pressures of 100 and 1000 mTorr are shown in Figs. 6 and 7, respectively. At 100 mTorr, the Ar* profile does not change appreciably as the applied voltage is varied between 75 V_{p-p} and 300 V_{p-p}. This agrees fairly well with the experiments. At this pressure, the electron mean free path is sufficiently long that changes in sheath thickness and electron heating resulting from higher power deposition does not appreciably affect the shape of the Ar* source function. At 1000 mTorr, decreasing the voltage below 150 V_{p-p} resulted in the Ar* profile becoming broader in the axial direction, although the peak remained at the same radial location. As we increased the voltage above 150 V_{p-p}, the Ar* profile collapsed to the lower electrode. A secondary peak appeared near the edge of the top electrode in the simulation which was not observed in the experiment. At the higher pressure, the mean free path of electrons is sufficiently short that the collapse of the sheath with increasing power deposition does affect the Ar* source function. Quenching of Ar* also increases due to the higher plasma density, thereby restricting the Ar* nearer to its site of generation.

McMillin and Zachariah[3] found that even a small amount of electron attaching gases can change the Ar* profile significantly. We investigated these trends by adding

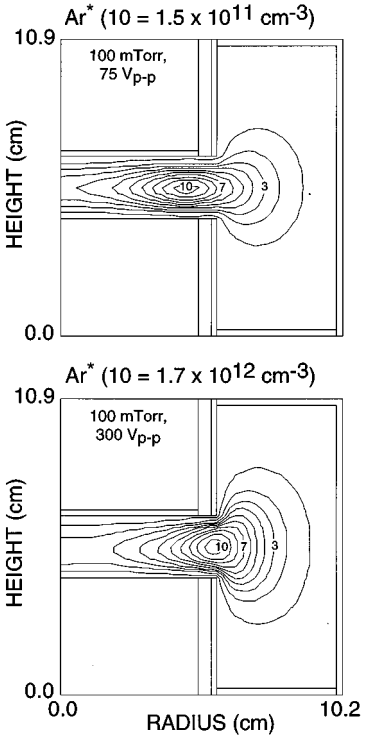

FIG. 6. Computed Ar* density in pure argon plasmas for a pressure of 100 mTorr: (a) 75 $V_{p\text{-}p}$ and (b) 300 $V_{p\text{-}p}$.

trace amounts of O_2 or CF_4 to Ar. The gas pressure was kept constant at 250 mTorr, the flow rate was 25 sccm, and the voltage was 200 V_{p-p} unless noted otherwise.

The computed Ar* density is shown in Fig. 8 for an

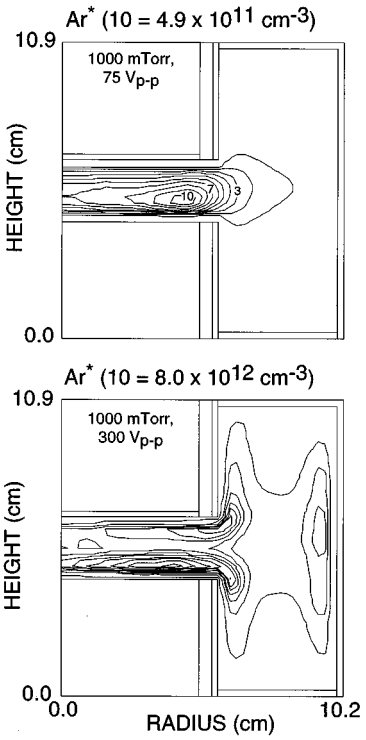

FIG. 7. Computed Ar* density in pure argon plasmas for a pressure of 1000 mTorr: (a) 75 $V_{p\text{-}p}$ and (b) 300 $V_{p\text{-}p}$.

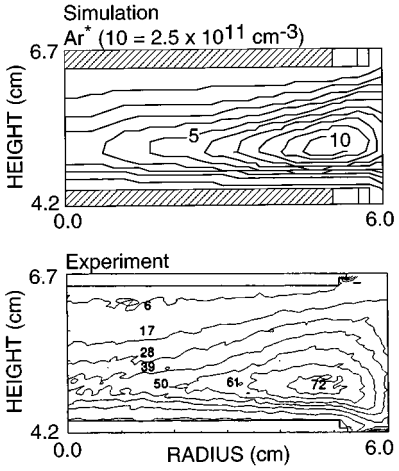

FIG. 8. Comparison of experimental and computed Ar* density profiles in an $Ar/O_2=98.8/1.2$ mixture at 250 mTorr and 200 $V_{p\text{-}p}$. The labels on the experimental contours are relative values.

$Ar/O_2=98.8/1.2$ mixture. The corresponding experimental result is also shown.[3] The model derived axial Ar* densities at the center line of the discharge are shown in Fig. 5(b). For the reasons cited earlier, at 250 mTorr the profile of Ar* density in pure argon is slightly skewed and the peak occurs close to the edge of the powered electrode at 250 mTorr. As O_2 is added to a fraction of 1.2%, the shape of the profile does not appreciably change. However, there is a decrease in the peak Ar* density which occurs mainly from quenching of Ar* by O_2 and O. There is a small shift in the peak Ar* density towards the power electrode with increasing O_2, although not significantly so. Although O_2 is a molecular attaching gas, the mean free path of sheath heated electrons above the excitation threshold of Ar($4s$) is little affected by admixtures of O_2, at least up to 2%. This may be a result of the resonant cross sections for vibrational excitation and attachment which are small at the energies which compete with excitation of Ar*. The tail of the distribution may also not be as cutoff as one expects in Ar/O_2 mixtures due to the local nature of the electron acceleration. One can define an ''energy loss'' Knudsen number as $K_n=d/\lambda_L=d\Sigma_i\sigma_i N_i$, where d is the distance over which electrons are accelerated, in this case the width of the sheath, λ_L is the mean free path for energy loss, σ_i is the energy loss cross section, and N_i is the gas density. If $K_n \gg 1$, then peak electron energies are essentially functions only of the acceleration mechanism, in this case sheath heating. If $K_n \ll 1$, then peak electron energies are largely a local function of the local E/N. For our conditions $K_n > 1$ and in adding a few percent O_2, K_n does not functionally change. Therefore the spatial distributions of the Ar* source functions also do not change, and so the Ar* profiles do not significantly change.

The Ar* density for $Ar/O_2=99.2/0.8$ at $V_{p-p}=75$ V and 300 V are shown in Fig. 9. At applied voltages less than 200 V_{p-p}, the Ar* profile does not appreciably change. The density, however, decreases with decreasing voltage as the plasma density decreases. As the voltage is increased beyond 200 V_{p-p}, the Ar* peak shifts towards the edge of the pow-

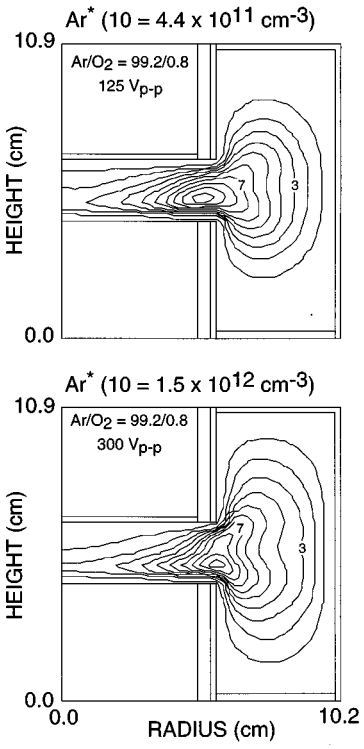

FIG. 9. Computed Ar* density for an $Ar/O_2=99.2/0.8$ mixture at 250 mTorr: (a) 125 V_{p-p} and (b) 300 V_{p-p}.

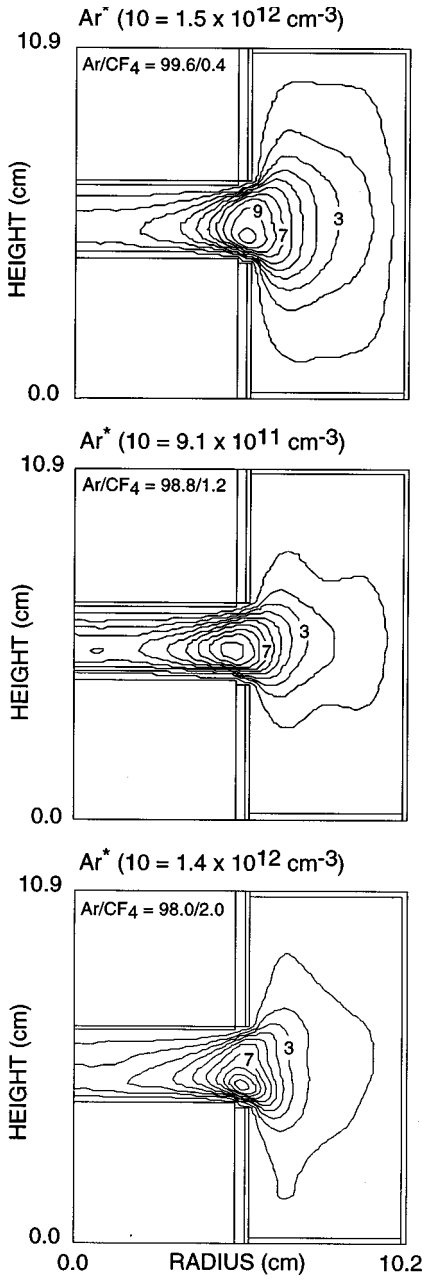

FIG. 10. Computed Ar* density in Ar/CF_4 discharges at 250 mTorr and 200 V_{p-p}. The CF_4 concentrations are (a) 0.4%, (b) 1.2%, and (c) 2.0%.

ered electrode. We will describe the cause of this change below.

The effects of adding CF_4 on the Ar* density profile are shown in Figs. 10 and 11. Addition of CF_4 produces less quenching than comparable amounts of O_2. At CF_4 concentrations of less than 0.8%, significant changes in the profile shapes were not experimentally observed. However, changes in profiles of Ar* can be observed at higher concentrations of CF_4. Experimentally the Ar* density decreased monotonically as CF_4 was added due to quenching. In our simulations, the Ar* density first decreased with increasing CF_4 concentration below 0.4%, increased for concentrations between 0.4% and 0.8%, and decreased at higher concentrations as shown in Fig. 5(c). While we have not been able to resolve this difference with the experiments, there are several probable reasons behind it. When CF_4 is added, our simulations show that two processes with opposite consequences take place. First, quenching causes a decrease in Ar* density. Second, there is a slight increase in electron temperature to compensate for the increased rate of attachment which will eventually increase the Ar* density. It is possible that these two processes are not being properly balanced at low CF_4 concentrations. Another possibility is boundary conditions. The reactive sticking coefficients for dissociation products have been estimated. The impact of, for example, F_2 formed by F atom recombination on the plasma chemistry is significant. F_2, even at small concentrations, is a larger source of attachment than CF_4.

As the CF_4 concentration is increased beyond 0.8%, the simulation results fall in line with experiments are shown in Fig. 11. In this regime, the addition of CF_4 leads to a decrease in Ar* density. This can be attributed to quenching by CF_4 and by C_2F_6 generated in the discharge. In addition to quenching, a change in the Ar* profile is observed as the peak in Ar* density shifts towards the edge of the powered electrode. At 3.6% CF_4, the peak is virtually at the edge.

Recall that the Ar* density profile shape changes when adding CF_4 while it remains virtually unmodified when O_2 is added. Both CF_4 and O_2 are electron attaching gases having comparable cross sections. The dissociation products, however, differ significantly in their attachment properties. In the case of F_2, the thermal attachment cross section exceeds 40 $Å^2$, whereas the CF_4 attachment cross section is resonant, has a threshold of 4.4 eV, and does not exceed 0.1 $Å^2$. Therefore, small amounts of F_2 greatly change the electrone-

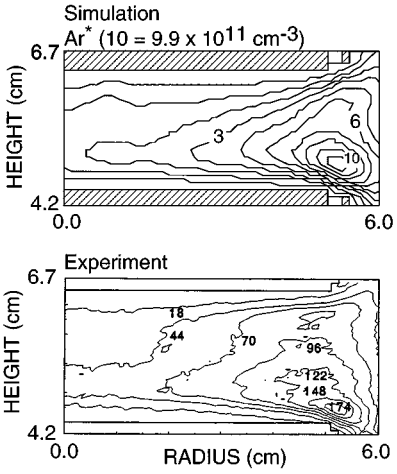

FIG. 11. Comparison of experimental and computed Ar* density profiles in an $Ar/CF_4=96.4/3.6$ mixture at 250 mTorr and 200 V_{p-p}. The labels on the experimental contours are relative values.

gativity of the plasma. On the other hand, any dissociation of O_2 (at low pressures) results in a reduction in the rate of attachment due to the low rate of attachment to O atoms.

F_2 is generated by electron impact dissociation of CF_4 producing F atoms followed by recombination on the walls, and by dissociative excitation transfer from Ar*. These processes generate a maximum F_2 density on the axis, as shown in Fig. 12. Electron loss due to attachment therefore also peaks on the axis, decreasing towards the outer radius. This produces a reduction in electron density at small radii, which in turn leads to the shift in the Ar* density peak towards the edge of powered electrode and depletion of Ar* in the center of the reactor. The major source of electron attachment in an Ar/O_2 plasma is O_2, which is uniformly distributed in the reactor at moderate applied voltages. Electron attachment, therefore, causes a spatially uniform loss of electrons. The relative number density of electrons available for electron impact excitation does not significantly change, and so the shape of Ar* density profile does not change. At large applied voltage, a significant amount of O_2 dissociates and the

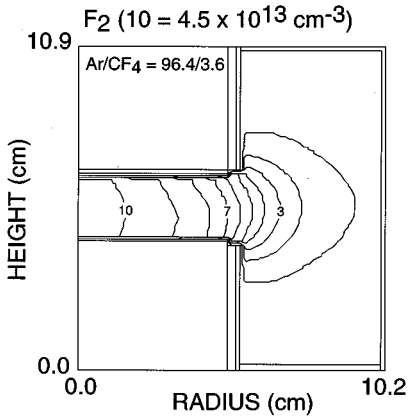

FIG. 12. Profile of F_2 density in an $Ar/CF_4=96.4/3.6$ plasma (250 mTorr 200 V_{p-p}).

O_2 profile becomes similar to the F_2 profile shown in Fig. 12. As a consequence, we observe similar Ar* profiles in Ar/O_2 at higher voltages (Fig. 9) as in Ar/CF_4.

IV. CHOICE OF THE APPROPRIATE MODEL

During this investigation, many permutations of the options for electron and heavy particle transport in the HPEM were used with the goal of reproducing experimental trends in both plasma density and Ar* profiles. We found, for example, that the experimental electron density as a function of pressure could be reproduced using the electron energy equation instead of the EMCS. However we were unable to reproduce the Ar* profiles. Similarly, when using the EMCS and computing Ar* densities using only the continuity equation with only diffusive transport (as opposed to including the momentum equations), experimental Ar* profiles were not reproduced. Quantitative agreement with experiments for both plasma density and the Ar* profiles over the range of pressures and gas mixtures we investigated required that the electron energy distribution (EED) be kinetically resolved using the EMCS, and that inertial effects be included for heavy particles (both neutral and charged) by solving their momentum equations.

We also found that quantitative agreement with experiments required fine resolution in both energy and space. Having a subcritical number of pseudoparticles in the EMCS did not sufficiently resolve the EED in the energy range where resonant attachment to O_2 and CF_4 occurs. Approximately five times the number of electron pseudoparticles were required in the Ar/O_2 and Ar/CF_4 mixtures as compared to the pure Ar cases.

In this particular rendition of the GECRC, the insulator and dark space shield are recessed by a few mm from the plane of the electrodes. Although the majority of the Ar* profiles could be captured in pure Ar and Ar/O_2 without resolving this ''ledge,'' it was necessary to resolve the feature in Ar/CF_4 mixtures to obtain agreement with experiments. We also found that the outer radius of the chamber affected the Ar* profiles. For example, decreasing the radius from 10 to 8 cm increased diffusion losses to the chamber wall sufficiently to perturb the Ar* profiles.

V. CONCLUDING REMARKS

In this article, we described results from simulations of Ar, Ar/O_2, and Ar/CF_4 plasmas in the GECRC. The major goal of these simulations was to investigate the mechanisms of Ar* generation and the consequences of varying applied voltage, pressure, and admixtures of reactive gases for the experimental conditions of McMillin and Zachariah's.[2–4] In general, the trends, magnitudes, and profile changes obtained in the simulations were in close agreement with experiments.

At low pressures in pure Ar, the Ar* density is axially symmetric and has a radial maximum near the edge of the electrodes. As the pressure was increased, the peak in Ar* density moved towards the powered electrode and the profile became skewed. These profiles were explained in terms of the shrinking sheath which increases electric field enhance-

ment at the edge of the electrodes, a decrease in electron mean free path, and an increase in quenching of Ar*.

In Ar/O_2 mixtures, addition of O_2 was found to only decrease the Ar* density, due to quenching of Ar* by O and O_2. The addition of O_2, at least up to 2%, does not appreciably change the energy-loss Knudsen number. When CF_4 was added to Ar, not only did the Ar density decrease due to quenching, but the profile also changed. The change in profile was attributed to a spatially inhomogeneous loss of electrons through attachment to dissociation products. We found that resolving both the proper magnitudes for electron densities and the Ar* profiles required a kinetic treatment for the electron energy distribution, and accounting for inertial effects for ions and neutrals.

ACKNOWLEDGMENTS

The work of S. Rauf was supported by the National Institute of Standards and Technology, and ARPA/AFOSR (F49620-95-1-0524). The work of M. Kushner was additionally supported by the National Science Foundation (ECS 94-04133) and the Semiconductor Research Corporation. The authors would like to thank Brian McMillin, Michael Zachariah, and James Whetstone for their insightful suggestions during this project.

[1] See special issue of: J. Res. Natl. Inst. Stand. Technol. **100**, 327–494 (1995).
[2] B. K. McMillin and M. R. Zachariah, J. Appl. Phys. **77**, 5538 (1995).
[3] B. K. McMillin and M. R. Zachariah, J. Appl. Phys. **79**, 77 (1996).
[4] B. K. McMillin and M. R. Zachariah, IEEE Trans. Plasma Sci. **24**, 113 (1996).
[5] L. J. Overzet and M. B. Hopkins, Appl. Phys. Lett. **63**, 2484 (1993).
[6] D. P. Lymberopoulos and D. J. Economou, J. Res. Natl. Inst. Stand. Technol. **100**, 473 (1995).
[7] P. L. G. Ventzek, M. Grapperhaus, and M. J. Kushner, J. Vac. Sci. Technol. B **12**, 3118 (1994).
[8] W. Z. Collison and M. J. Kushner, Appl. Phys. Lett. **68**, 903 (1996).
[9] M. J. Kushner, W. Z. Collison, M. Grapperhaus, J. P. Holland, and M. S. Barnes, J. Appl. Phys. **80**, 1337 (1996).
[10] S. Rauf and M. J. Kushner, J. Appl. Phys. **81**, 5966 (1997).
[11] T. Holstein, Phys. Rev. **83**, 1159 (1951).
[12] L. J. Overzet, J. Res. Natl. Inst. Stand. Technol. **100**, 401 (1995).
[13] K. Tachibana, Phys. Rev. A **34**, 1007 (1986).
[14] D. Rapp and P. Englander-Golden, J. Chem. Phys. **43**, 1464 (1965).
[15] R. H. McFarland and J. D. Kinney, Phys. Rev. **137**, A1058 (1965).
[16] P. K. Leichner and R. J. Ericson, Phys. Rev. A **9**, 251 (1974).
[17] A. V. Phelps, JILA Information Center Report No. 28, University of Colorado (1985).
[18] J. B. A. Mitchell, Phys. Rep. **186**, 215 (1990).
[19] R. R. Laher and F. R. Gilmore, J. Phys. Chem. Ref. Data **19**, 277 (1990).
[20] R. E. Olson, J. R. Peterson, and J. Moseley, J. Chem. Phys. **53**, 3391 (1970).
[21] D. L. Albritton, At. Data Nucl. Data Tables **22**, 1 (1978).
[22] Y. Ikezoe, S. Matsuoka, M. Takebe, and A. Viggiano, *Gas-Phase Ion-Molecule Reaction Rate Constants Through 1986* (Maruzen, Tokyo, 1987).
[23] D. L. Baulch, R. A. Cox, P. J. Crutzen, R. F. Hampson, J. A. Kerr, J. Troe, and R. T. Watson, J. Phys. Chem. Ref. Data **11**, 327 (1982).
[24] J. A. Davidson, H. I. Schiff, G. E. Streit, J. R. McAfee, A. L. Schmeltekopf, and C. J. Howard, J. Chem. Phys. **67**, 5021 (1977).
[25] D. C. Parent, R. Derai, G. Mauclaire, M. Heninger, R. Marx, M. E. Rincon, A. O'Keefe, and M. T. Bowers, Chem. Phys. Lett. **117**, 127 (1985).
[26] P. Gaucherel, Int. J. Mol. Spec. **25**, 211 (1977).
[27] L. G. Piper, J. E. Velazco, and D. W. Setser, J. Chem. Phys. **59**, 3323 (1973).
[28] D. L. King, L. G. Piper, and D. W. Setser, J. Chem. Soc. Faraday Trans. **73**, 177 (1977).
[29] R. A. Bonham, Jpn. J. Appl. Phys., Part 1 **33**, 4157 (1994).
[30] M. Hayashi, in *Gaseous Dielectrics V*, edited by L. G. Christophorou and D. W. Bouldin (Pergamon, New York, 1987).
[31] M. Hayashi and T. Nimura, J. Appl. Phys. **54**, 4879 (1983).
[32] G. K. Vinogradov, P. I. Verzorov, L. S. Polak, and K. I. Slovetsky, Vacuum **32**, 592 (1982).
[33] E. Fisher, M. E. Weber, and P. B. Armentrout, J. Chem. Phys. **76**, 4932 (1982).
[34] J. E. Velazco, J. H. Koltz, and D. W. Sester, J. Chem. Phys. **65**, 3468 (1976).
[35] K. Okada, O. Kajimoto, and T. Fueno, B. Chem. Soc. Jpn. **51**, 443 (1978).
[36] E. L. Keating and R. A. Matula, J. Chem. Phys. **66**, 1237 (1977).
[37] K. R. Ryan and J. C. Plumb, Plasma Chem. Plasma Process. **6**, 231 (1986).